ROYAL SOCIETY
OF CHEMISTRY

PAPER

Check for updates

A computational study on boron dipyromethene ancillary acceptor-based dyes for dye-sensitized solar cells†

Ganapathi Rao Kandregula,[a] Sudip Mandal, [ID][ab] Gollapalli Prince, [ID][c] Satyesh Kumar Yadav [ID][c] and Kothandaraman Ramanujam [ID] *[ad]

A series of (D-π)$_2$–A$_n$–A based organic dyes containing a boron dipyrromethene (BODIPY) moiety as an ancillary acceptor (A$_n$) derivative were chosen, and the effect of donor moieties (diarylamine, carbazole, azepine, and dibenzazepine) was investigated to understand their photophysical and photoelectrochemical properties by employing density functional theory (DFT) and time-dependent DFT. It is experimentally proved that BODIPY enhances light-harvesting in the red and near IR regions of visible light. Electron density distribution analysis was performed for all the dyes to confirm the intramolecular charge transfer, envisioned from the simulated absorption spectra of the dyes. Carbazole donor-based dyes exhibited the lowest reorganization energy. A dye attached to the TiO$_2$(1 0 1) surface was modeled to estimate the adsorption energy of the dyes. The density of states analysis revealed that the absence of defect states in the bandgap of TiO$_2$ facilitates smooth electron transfer from the excited state of the dye to the conduction band of TiO$_2$. Considering the lowest unoccupied molecular orbital (LUMO) energy level of the dyes and the conduction band energy level of TiO$_2$, it is understood that all the dyes studied in this report are capable of electron injection upon photoexcitation. Considering the driving force for dye regeneration and the magnitude of reorganization energy, a carbazole donor-based dye (D2) would be the best performing dye in DSSCs. Previously, the power conversion efficiencies of the dyes have been reported, and the carbazole donor-based dye (D2) exhibited the highest efficiency among all the dyes. Our computational investigations are in good agreement with the experimental results.

Introduction

The global energy demand is increasing rapidly with the current pace of technology growth. To keep in check the alarming environmental impact of fossil fuel, energy production from renewable resources, such as converting solar energy into electricity, is a prominent solution.[1] Various solar photovoltaic (PV) technologies have been explored, such as crystalline silicon,[2–4] dye-sensitized solar cells (DSSCs)[5,6] thin-film technologies (CIGS),[2,7] and perovskite solar cells,[8,9] among these DSSCs have

gained substantial attention due to their ease of fabrication, cost-effective manufacturing technology, and environmental benignity.[10] DSSCs allow the fabrication of flexible and semi-transparent cells virtually in any color. Moreover, the ability of DSSCs to operate in diffuse light conditions, with high power conversion efficiency (PCE) in comparison to their performance under 1 sun conditions, makes them suitable for indoor operation.[11]

Panchromatic absorption, tapping into the IR radiation of the sun's spectrum along with the entire visible region, is one of the ways to improve the PCE of DSSCs.[12–14] For the same reason, boron dipyrromethene (BODIPY) (4,4-difluoro-4-bora-3a,4a-diazaindacene) based dyes were examined in DSSC applications.[15–22] Reports on the use of BODIPY dyes in DSSCs are scarce, despite their popularity for more than a decade as biomolecular labeling, sensing, and logic gate design materials.[23,24] Intense research on the molecular engineering of BODIPY, to tune its optical and electrochemical properties, is proceeding owing to the versatility of BODIPY.

BODIPY based dyes were explored for DSSCs because of their high quantum yields, excellent molar extinction coefficients

[a] *Department of Chemistry, Indian Institute of Technology Madras, Chennai, 600 036, India. E-mail: rkraman@iitm.ac.in*

[b] *Division of Chemistry, Department of Sciences and Humanities, Vignan's Foundation for Science, Technology and Research, Vadlamudi, Guntur, Andhra Pradesh, 522 213, India*

[c] *Department of Metallurgical and Materials Engineering, Indian Institute of Technology Madras, Chennai, 600 036, India*

[d] *DST-IITM Solar Energy Harnessing Centre, Indian Institute of Technology Madras, Chennai, 600 036, India*

† Electronic supplementary information (ESI) available. See DOI: 10.1039/c9nj05334d
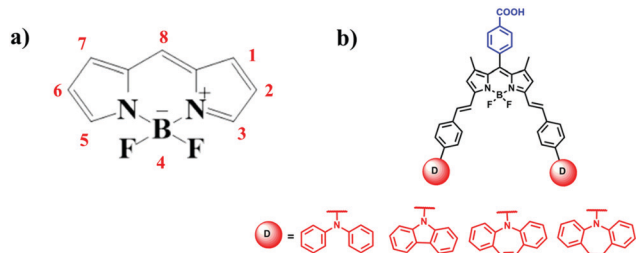
Fig. 1 (a) Typical structure of a BODIPY (numbering according to the IUPAC nomenclature) (b) The chemical structure of a dye molecule, D representing donor moieties, *viz.*, diarylamine, carbazole, azepine, and dibenzazepine from left to right and the corresponding dyes are named D1, D2, D3, and D4, respectively.

across the visible and near-IR regions and relatively long excited-state lifetimes.[25] Hattori *et al.* reported the first BODIPY based sensitizer, 8-(2,4,5-trimethoxyphenyl)-4,4-difluoro-1,3,5,7-tetramethyl-4-bora-3*a*,-4*a*-diaza-*s*-indacene (MEOPHBDP), in 2005 for DSSCs.[15] They have modified the BODIPY-based donor–acceptor dyad at its C-8 position using an electron-donating 2,4,5-trimethoxyphenyl moiety (Fig. 1a). This dye achieved a PCE of 0.16%, and the lower PCE is due to the aggregation of dyes onto the TiO_2 surface. Kolemen *et al.* synthesized a dye with cyanoacetic acid and 4-(diphenylamino)phenyl groups as electron-withdrawing/anchoring and electron-donating groups, respectively. According to the authors, panchromatic absorption of the dye was a result of extending the conjugation using styryl substituents at its C-3 and C-5 positions (shown in Fig. 1a). Although they could achieve panchromatic absorption, the PCE was only 0.68%[19] because of the weak electron injection of this dye from its excited state to the conduction band (CB) of TiO_2. Galateia *et al.* employed another approach by introducing two BODIPY moieties covalently attached to a 1,3,5-triazine molecule on a carboxyphenyl meso-substituted porphyrin core and constructed a triad, PorCOOH-(BDP)$_2$. In this triad, BODIPY, 1,3,5-triazine, and carboxyphenyl *meso*-substituted porphyrin act as a donor, π-linker, and an acceptor unit, respectively. The dye exhibited strong absorption at around 500 nm, which is attributed to the absorption band corresponding to the BODIPY moiety.[26] The introduction of BODIPY units enhanced not only the spectral response but also the alignment of energy levels for efficient electron injection and dye regeneration. The PorCOOH-(BDP)$_2$ dye exhibited PCEs of 5.17% with pristine TiO_2 semiconductor films of 12 μm thickness, and it further improved to 6.20% when rGO/TiO_2 was used as the semiconductor material. The incorporation of rGO between TiO_2 and PorCOOH-(BDP)$_2$ formed a Schottky barrier in the device, which led to efficient charge transport of the injected electrons. Kubo *et al.* reported three BODIPY based dyes (dye 1–3) with thienyl-cyanoacrylic acid acceptor units for DSSC application.[22] These dyes exhibited a strong absorption band in the longer wavelength region. The dye having a butterfly-shaped structure (dye 2) showed improved intramolecular charge transfer and achieved the highest PCE of 6.06% due to its excellent light harnessing ability and higher LUMO energy level, which helped in effective electron injection into the CB of TiO_2. Recently, Rao *et al.*

reported NIR absorbing Aza-Bodipy based small molecules, which exhibited the highest efficiency among BODIPY based dyes.[27] In their study, they have covalently coupled phenothiazine and phenoxazine moieties to Aza-Bodipy to obtain AZA-PTZ-BOD and AZA-POZ-BOD dyes, respectively. The AZA-PTZ-BOD and AZA-POZ-BOD dye-based organic solar cells exhibited PCEs of 8.23% and 7.24%, respectively. The panchromatic absorption (300 to 1000 nm wavelength), suitable photonic properties, balanced charge transport, efficient exciton dissociation, and reduced bimolecular recombination make AZA-PTZ-BOD dye achieve a higher value of short-circuit current density and fill factor and hence the resultant power conversion efficiency.[27] Table S1 (ESI†) shows a comparison of the electrical performance of all the BODIPY based dyes known for OPV and DSSC applications.

In this study, we have considered four BODIPY-based dye molecules, which are experimentally studied and reported earlier by Zhang *et al.*[28] Density functional theory (DFT) and time-dependent DFT (TD-DFT) studies have been employed to correlate the structure–property relationship of the BODIPY based dyes. Our motivation to undertake this work is to understand the energy level alignment of the dyes while changing the various donor units and to study their photophysical properties at the molecular level, which is not reported by Zhang *et al.*[28] The effect of different donor moieties attached to the BODIPY[29–32] core has been focused in the current study using first principles calculations.[33–40]

Model and computational details

The optimization of ground-state geometries of the isolated dyes was carried out using the Gaussian 09 program package[41] with the hybrid meta-GGA M06-2X functional[42] using the polarized split-valence 6-31G(d,p) basis set.[43,44] The molecular structure of the dyes was drawn using the GaussView 5.0 visualization program, and the excited state properties of the dyes were analyzed using the GussSum 3.0 software.[45] The frequency calculation was performed to check the stationary nature of the optimized geometries at the energy minimum at the same level of theory. The solvent effect was employed by using an integral equation formalism polarizable continuum model (IEF-PCM) with dichloromethane (DCM) as a solvent (dielectric constant, $\varepsilon = 8.93$).[46] The highest occupied molecular orbital (HOMO), the LUMO, and the HOMO–LUMO energy gap have been estimated from the optimized ground state geometry, and Kohn–Sham frontier orbital analysis was performed using the optimized structures.[47,48] TD-DFT calculations have been performed to understand the photophysical properties of the dyes such as the excitation energies corresponding to the vertical transition from the ground state to the excited state, oscillator strengths (f), and the contributions of the molecular orbitals responsible for the transition and their percentage of composition.[34]

To understand the interaction of dye and TiO_2 systems, first-principles calculations based on DFT were carried out as implemented in the Vienna Ab initio simulation package (VASP)[49,50]

code using the Perdew, Burke, and Ernzerhof (PBE) generalized gradient approximation (GGA) as the exchange–correlation functional.[51,52] The pseudopotential was based on the projector-augmented wave (PAW) method[53,54] that explicitly includes the following valence configurations for different elemental species: $3s^2\,3p^6\,4s^2\,3d^2$ ($12e^-$) for Ti, $2s^2\,2p^4$ ($6e^-$) for O, $2s^2\,2p^2$ ($4e^-$) for C, $1s^1$ ($1e^-$) for H, $2s^2\,2p^3$ ($5e^-$) for N, $2s^2\,2p^1$ ($3e^-$) for B, and $2s^2\,2p^5$ ($7e^-$) for F. Brillouin zone sampling was done using the Monkhorst–Pack scheme of k-points with gamma centered meshes. We used $6 \times 6 \times 4$ and $1 \times 2 \times 1$ k-points for bulk and slab of anatase $TiO_2(1\,0\,1)$ calculations, respectively. In all our calculations, a plane wave kinetic energy cutoff of 520 eV was used, and an energy convergence of 1 meV per atom was ensured.

The photovoltaic properties of DSSCs strongly depend on the orientation of the dye on the surface of the semiconductor and the reconstructions of the semiconductor surface owing to the dye attachment. Previous reports established that the anatase phase of TiO_2 is better than rutile and brookite phases on photocatalytic activity, short-circuit photocurrent, electron transport, and dye loading.[55,56] The most stable surface of TiO_2, anatase, is established as the (1 0 1) surface, modeled using a slab containing 80 'Ti' and 160 'O' atoms: the in-plane dimension of a supercell is x-direction $\times$ y-direction. The aspects of the supercell are such that the distance between periodically repeating dyes is more than 10 Å in any direction.

Results and discussion

Designed structures

The chemical structures of BODIPY-based dyes (D1 to D4) are shown in Fig. 1. Diarylamine, carbazole, azepine, and dibenz-azepine act as donor moieties, a styryl unit acts as a π-bridge between the donor and the BODIPY moiety, and benzoic acid acts as an acceptor moiety. Two donor-π-linker moieties are attached to the BODIPY unit, making a $(D\text{-}\pi)_2\text{-}A_n\text{-}A$ configuration (where A_n = BODIPY). The structure of the dye molecule

forms a Y like shape. The ground state optimized geometries of the dyes are shown in Fig. 2.

Alignment of energy levels and driving force for dye regeneration

The benchmark study has been performed using various functional with different basis sets, and the outcome of this analysis is presented in Table S2 (ESI†). HOMO energy (E_H), LUMO energy (E_L), and driving force for dye regeneration are reported in Table S2 (ESI†). E_H, E_L, and driving force for dye regeneration calculated using M06-2X/6-31G(d,p) seem to be the closest match to the experimental data.

The energy level diagram of the four dyes, along with the energy level of the CB of TiO_2 and the redox energy level of the electrolyte, is given in Fig. 3. Table 1 lists the calculated E_H, E_L, and energy gap between the HOMO and the LUMO ($E_{H\text{–}L}$), and the experimental values (adapted from the work of Zhang $et\ al.$[28]) are also mentioned in the parentheses next to the theoretical values. A small variation between the theoretical and experimental values is mainly due to the exclusion of the solid-state packing effect in our model. The calculation of energy levels of organic dye molecules includes the optimization of an isolated dye with the incorporation of an implicit solvent medium. This model does not take into account the molecular aggregation between the dye molecules and other parameters, such as the electrochemical interface between the dye molecule and the electrode while measuring the ground state potential. The incorporation of such parameters makes the computational calculations very expensive and complex as well. Therefore, in this study, we tried to probe the trend of the energy levels with the experimental data. The parameters for the optimized ground and excited state geometries are tabulated in Tables S3–S6 (ESI†). It is to be noted that the bond length and the bond angle have been modified a bit (in terms of increment or decrement) in the excited state structure in comparison to that of the ground state structure. The frequency calculations were performed for both ground and excited state
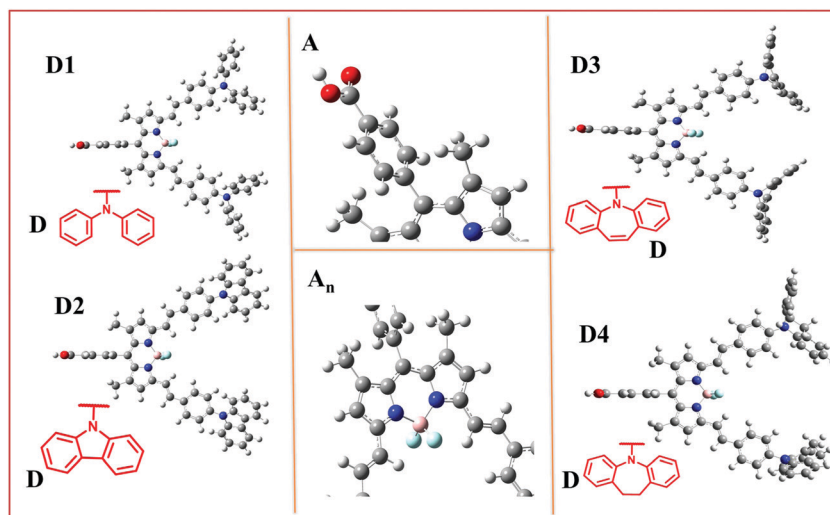

Fig. 2   The optimized structures of the dyes obtained using the M06-2X/6-31G(d,p) method.
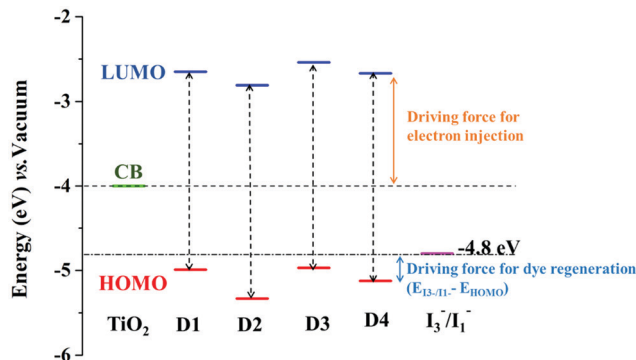
Fig. 3 The energy level diagram of four dyes, including the conduction band of TiO$_2$ and the redox potential energy level of the I$_3^-$/I$^-$ couple.

Table 1 HOMO, LUMO, bandgap energy, and driving force for dye regeneration (in eV) calculated using the M06-2X/6-31G(d,p) method. The experimental values are given in parentheses

Dyes	E_H/eV	E_L/eV	E_{H-L}/eV	Driving force for dye regeneration $(E_{I_3^-/I^-} - E_H)$/eV
D1	−4.99 (−5.06)	−2.65 (−3.41)	2.34 (1.74)	0.19
D2	−5.33 (−5.30)	−2.81 (−3.52)	2.52 (1.89)	0.53
D3	−4.97 (−4.98)	−2.54 (−3.30)	2.43 (1.75)	0.17
D4	−5.12 (−4.96)	−2.67 (−3.31)	2.45 (1.74)	0.32

geometries and are tabulated in Table S7 (ESI†). The absence of an imaginary frequency confirms the stationary nature of the optimized geometries at the energy minimum.

The energy level of the LUMO of all the dyes is higher than that of the CB of TiO$_2$ (−4.0 eV vs. vacuum), which facilitates the electron injection from the LUMO of the dye to the CB of TiO$_2$. Similarly, the energy level of the HOMO should be located below the redox potential energy of the I$_3^-$/I$^-$ electrolyte for the sufficient driving force for dye regeneration (Fig. 3).

The HOMO energy levels of D1 (−4.99 eV), D2 (−5.33 eV), D3 (−4.97 eV), and D4 (−5.12 eV) are below the redox potential energy (−4.80 eV vs. vacuum) of the I$_3^-$/I$^-$ electrolyte. Moreover, the HOMO energy levels for D1 and D3 are slightly higher in comparison to those of the other dyes, which indicates that their HOMO level has been destabilized due to the introduction of diarylamine and azepine, respectively. For an efficient DSSC, regeneration of the dye from its cationic to neutral form is essential for continuous cell operation. Besides dye regeneration, driving force can impact the kinetics of back-electron transfer between the injected electrons in the CB of TiO$_2$ with the oxidized dye and I$_3^-$.

The calculated dye regeneration driving force of the four dyes is in the following increasing order: D3 (0.17 eV) < D1 (0.19 eV) < D4 (0.32 eV) < D2 (0.53 eV), and Zhang et al.[28] reported the photovoltaic performance of the four dyes (D1 to D4), and among them, D2 showed the highest electrical performance, which could be due to the higher driving force for dye regeneration of D2. The driving force for dye regeneration is higher for D2 as compared with the other dyes, which is reflecting the higher performance of this dye in the DSSC mode. These data matched well with the experimental result.

Electron density distribution analysis

The electron density distribution analysis was performed by calculating the population of electron density on each energy level, including ground and virtual states using the M06-2X/6-31G(d,p) level of theory. It provides quantitative evidence about the localization of electron density at different parts of the dye, such as the donor, the π-linker, and the acceptor. The existence of ICT in the dyes during photoexcitation can be clarified by finding the relative ordering of occupied and virtual orbitals, i.e., the HOMO and LUMO of the dyes. The outcome of this analysis of the four dyes is presented in Table 2 (HOMO−1, HOMO, LUMO, and LUMO+1).

During photoexcitation of a dye, the electron density in the donor moiety shifts to the virtual orbital located on the acceptor part, which is called as ICT. It is comprehended that for all the four dyes, the electron density at the HOMO (35 to 99% in the donor and 0.08 to 20% in the π-linker) shifts to the LUMO (15 to 20% in the π-linker and 53 to 65% in the acceptor). This indicates that during ICT, some amount of electron density remained on the π-linker moiety, which is well established through the frontier orbital diagram of dyes shown in Fig. 4. In all the dyes, the electron density at the HOMO is delocalized over the donor moiety and partly on the π-linker, while the electron density at the LUMO is mainly delocalized on the π-linker and the acceptor. The overlap between HOMOs and LUMOs is reasonably good, which favors efficient electron transfer from the donor of the dyes to the CB of TiO$_2$.

Electronic absorption spectra

DSSCs convert sunlight into electricity, so it is crucial to gain insight into the excited state properties of the dyes for a better understanding of the electronic structure and light-harvesting efficiency. The electronic spectra simulation using TD-DFT was carried out using various functionals. The benchmark study of the functionals has been performed by including two basis sets with different functionals. The excited-state properties of the

Table 2 The projected density of states (PDOS) analysis of four dyes obtained using the M06-2X/6-31G(d,p) method

| Dye	Composition	HOMO−1	HOMO	LUMO	LUMO+1
D1	Donor	85.69	49.90	16.47	0.01
	Linker	7.14	16.72	17.36	0.04
	Ancillary acceptor (BODIPY)	6.92	33.30	64.58	3.10
	Acceptor	0.25	0.08	1.59	96.84
D2	Donor	93.21	34.98	15.22	0.09
	Linker	3.59	19.43	18.23	0.11
	Ancillary acceptor (BODIPY)	3.08	45.49	64.94	3.19
	Acceptor	0.12	0.10	1.61	96.61
D3	Donor	99.95	36.72	15.32	0.02
	Linker	0.03	20.40	17.70	0.04
	Ancillary acceptor (BODIPY)	0.02	42.73	65.38	3.11
	Acceptor	0	0.15	1.60	96.83
D4	Donor	99.89	38.27	15.42	0.02
	Linker	0.06	20.00	17.77	0.05
	Ancillary acceptor (BODIPY)	0.05	41.58	65.20	3.11
	Acceptor	0	0.15	1.60	96.82
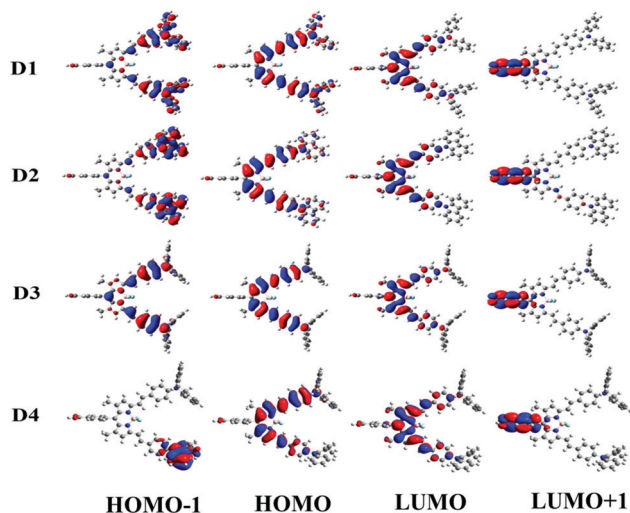
Fig. 4 Frontier molecular orbitals (HOMO−1 to LUMO+1) of the dyes obtained using the M06-2X/6-31G(d,p) method.

dyes with various functionals and basis sets are tabulated in Table S8 (ESI†). For D1 and D2, the PBE1PBE/6-31+G(d,p) method is found to be more suitable for defining the charge transfer band, whereas for D3 and D4, TPSSH/6-31+G(d,p) is found to exhibit a closer match with the experimental data. The inclusion of the diffusion function for the calculation of electronic spectra was incorporated to comprehend the charge transfer behavior. It has improved the charge transfer behavior and exhibits a close match with the experimental UV-Vis spectra. The simulated electronic absorption spectra are presented in Fig. 5. Two distinct peaks are observed in the absorption spectra, wherein the peak located between 350 and 550 nm is denoted as the π–π* transition (Frontier molecular orbitals that involved π–π* transition are shown in Fig. S1–S4, ESI†) from the aromatic organic framework, and another peak beyond 550 nm represents ICT due to the charge transfer from the donor to the acceptor moiety. More detailed information in terms of the maximum absorption wavelength (λ_c), the oscillator strength (f), and the percentage of transition probability from the occupied to the virtual orbitals is
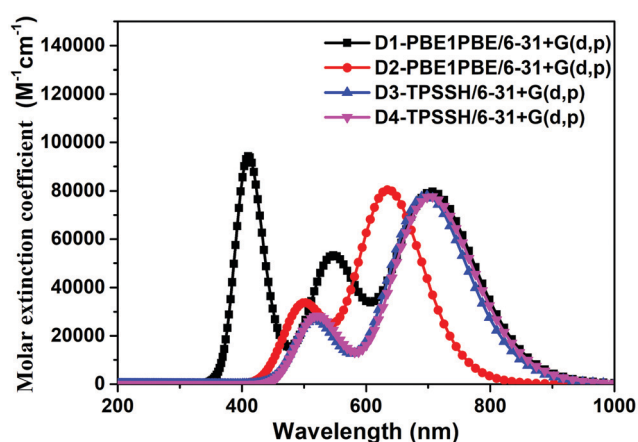

Fig. 5 Computed UV-Vis absorption spectra of four dyes in DCM solvent.

tabulated in Table 3. λ_c values are in the decreasing order of D2 < D3 < D4 < D1. The poor coplanarity between the carbazole donor unit and the BODIPY moiety in D2 causes a blue-shift in the absorption band in the range of 500–800 nm.

In D2, the carbazole moiety and BODIPY unit are non-coplanar (dihedral angle is 48°) with each other, and the carbazole unit itself is in a twisted configuration. In the cases of D3 and D4, the twist (bending) in the donor part does not exist because of the presence of a seven-membered ring which is somewhat coplanar with the BODIPY moiety. Hence, D2 bearing a rigid carbazole unit inhibits intermolecular π–π aggregation when compared to D1, D3, and D4, and hence D2 exhibited the highest performance in DSSCs.

Reorganization energy calculation

The amount of energy cost owing to the conformational reorganization of molecules caused by photoexcitation is defined as the reorganization energy of the dye molecule. Based on the Marcus electron transfer theory,[57] the kinetics of the electron transfer rate could be affected by reorganization energy from the following equation:

$$k_{\text{ET}} = \frac{1}{\sqrt{\Lambda_{\text{total}}}} \sqrt{\frac{\pi}{\hbar^2 k_{\text{B}} T}} |V^2| \exp\left\{ -\frac{\Lambda_{\text{total}}}{4 k_{\text{B}} T} \right\} \quad (1)$$

From eqn (1), it is to be noted that except the total reorganization energy (Λ_{total}), all other parameters on the right-hand side are constant. Hence, the rate constant for electron transfer (k_{ET}) entirely depends only on Λ_{total}. Λ_{total} is the sum of the electron (Λ_{e}) and the hole reorganization (Λ_{h}) energies, which can be calculated using the following equations:

$$\Lambda_{\text{e}} = (E_{\text{n}^-} - E_{\text{a}}) + (E_{\text{a}}^0 - E_{\text{n}}) \quad (2)$$

$$\Lambda_{\text{h}} = (E_{\text{n}^+} - E_{\text{c}}) + (E_{\text{c}}^0 - E_{\text{n}}) \quad (3)$$

$$\Lambda_{\text{total}} = \Lambda_{\text{e}} + \Lambda_{\text{h}} \quad (4)$$

where E_{n}, E_{c}, and E_{a}, represent the total energies of the neutral, cation, and anion systems, respectively, at their corresponding optimized geometries. E_{n^+} (E_{n^-}) is the energy of the cation (anion) at their optimized neutral molecules and E_{c}^0 (E_{a}^0) is the energy of the neutral molecules computed from the optimized cationic (anionic) geometries.

Λ_{total} is a measure of the energy penalty due to the geometry modification of the dye molecule during ICT from the donor to the acceptor. In general, the reorganization energy comprises internal and external reorganization energies. The external reorganization energy represents the effect of the solvent medium during the charge transfer, and the internal reorganization energy deals with the structural rearrangement between neutral and ionic states. In our calculation, we have concentrated on the internal reorganization energy to understand the mobility of the charge carriers. For achieving greater electron injection, i.e., to obtain higher current density, the Λ_{total} value must be smaller.

Table 4 summarizes the calculated Λ_{e}, Λ_{h}, and Λ_{total} of all dyes. The highest Λ_{total} of D4 and D3 leads to a lower electron injection ability, which is connected to a poor PCE in DSSCs.

Table 3 Computed absorption wavelengths (λ_c, in nm), electronic transitions, and oscillator strengths (f) for the singlet–singlet transitions for metal-free organic dyes in DCM solvent medium. λ_{max} represents the experimentally measured maximum absorption wavelength in the DCM solvent

Dye	λ_{max}/nm Experimental	States	λ_c/nm Theory	Functional/basis set	Oscillator strength (f)	Major Transition (%)
D1	693.5	S_0 to S_1	706	PBE1PBE/6-31+G(d,p)	1.096	HOMO to LUMO (99%)
	347.5	S_0 to S_2	546		0.7275	HOMO−1 to LUMO (98%)
		S_0 to S_3	409		1.2812	HOMO to LUMO+2 (94%)
D2	644.5	S_0 to S_1	635	PBE1PBE/6-31+G(d,p)	1.1083	HOMO to LUMO (99%)
	347.5	S_0 to S_2	503		0.4251	HOMO−1 to LUMO (98%)
		S_0 to S_3	466		0.0731	HOMO−2 to LUMO (99%)
D3	695	S_0 to S_1	696	TPSSH/6-31+G(d,p)	1.0417	HOMO to LUMO (96%)
	347	S_0 to S_2	517		0.2105	HOMO−2 to LUMO (50%), HOMO to LUMO+1 (42%)
		S_0 to S_3	461		0.0103	HOMO−3 to LUMO (87%)
D4	700	S_0 to S_1	704	TPSSH/6-31+G(d,p)	1.0494	HOMO to LUMO (95%)
	347	S_0 to S_2	672		0.0269	HOMO−1 to LUMO (98%)
		S_0 to S_3	520		0.3598	HOMO−2 to LUMO (85%)

Table 4 The calculated electron reorganization energy (Λ_e), hole reorganization energy (Λ_h), and total reorganization energy (Λ_{total}) of metal-free organic dyes (D1 to D4) obtained using the M06-2X/6−31G(d,p) method

Dyes	Λ_e/eV	Λ_h/eV	Λ_{total}/eV
D1	0.36	0.28	0.64
D2	0.26	0.22	0.48
D3	0.28	0.59	0.87
D4	0.29	0.60	0.89

The increasing order of Λ_{total} is D2 < D1 < D3 < D4. D2 exhibited the lowest Λ_{total}, which would enhance the rate of electron transfer from the excited state of the dye to the CB of TiO$_2$, which manifests the highest PCE in DSSCs (Table 4). Hence, the obtained Λ_{total} values of dyes can be considered to predict the trend in the electron injection efficiency among the four dyes qualitatively.

The excited-state lifetime of the dyes was calculated using the following equation:

$$\tau = \frac{1.499}{(fE^2)} \qquad (5)$$

where E is the excitation energy (in cm^{-1}) of the first excited states and f is the oscillator strength for the corresponding state.[58–60] The lifetime values for all the dyes are presented in Table 5. The dye possessing a higher first excited state lifetime is predicted to transfer charge efficiently. The calculated results show that all four dyes almost exhibit similar excited state lifetimes.

Table 5 Calculated excited-state lifetimes and radiative and non-radiative decay rates of the dyes

Dyes	τ/ns	$\varphi_f{}^a$	K_r/s^{-1}	K_{nr}/s^{-1}
D1	6.83	0.013	1.90×10^6	1.45×10^8
D2	5.47	0.516	94.30×10^6	0.88×10^8
D3	6.98	0.022	3.15×10^6	1.40×10^8
D4	7.08	0.140	1.97×10^6	1.21×10^8

^{a} φ_f is taken from the experimental data reported by Zhang *et al.*[28]

Based on the reorganization energy and the reasonable higher excited-state lifetime, D2 would be the best performing dye for DSSCs as compared with the other dyes.

The radiative decay rate (K_r) and non-radiative decay rate (K_{nr}) of the dyes are calculated using lifetime values and experimental quantum yield (φ_f). K_r values are found to be in the order D2 > D4 > D3 > D1, whereas K_{nr} values are found to be in the order D2 < D4 < D1 ≈ D3. Non-radiative decay can be described as the loss of thermal energy due to the rotation of aryl substituents in the excited state. The time scale for the non-radiative decay process is in the pico-second range, whereas for the radiative decay process, it is in the nanosecond scale. Hence the non-radiative process is faster than the radiative decay process. The blocking of free rotation would decrease the rate of non-radiative decay and, as a result, lead to higher electron injection into the conduction band of TiO$_2$. As per the following quantum yield equation, higher radiative decay and smaller non-radiative decay result in higher photovoltaic performance. D2 exhibits the lowest K_{nr} among the four dyes due to the fused benzene ring in the carbazole group.

$$\tau = \frac{\varphi_f}{K_r} \qquad (6)$$

$$\varphi_f = \frac{1}{1 + \dfrac{K_{nr}}{K_r}} \qquad (7)$$

Photovoltaic parameters pertaining to DSSC performance

The overall PCE (η) of a DSSC is the ratio of the output electrical power to the input light power. Thus η can be calculated using eqn (8).

$$\eta\,(\%) = \frac{V_{OC} \times J_{SC} \times FF}{I_{input}} \times 100 \qquad (8)$$

where J_{SC} and V_{OC} are the short-circuit current density and open-circuit voltage, respectively. $V_{OC} \times J_{SC} \times FF$ is the area under the I–V curve. FF is the fill factor or ideality factor, which

depends on the series and shunt resistance of the cell, and I_{input} is the incident power density. J_{SC} can be represented as in eqn (9).

$$J_{SC} = \int_{\lambda} LHE(\lambda) \Phi_{inject} \eta_{collect} \, d\lambda \qquad (9)$$

where $LHE(\lambda)$ is the light-harvesting efficiency at a specific wavelength (associated with f), which is provided in the equation,

$$LHE = 1 - 10^{-f} \qquad (10)$$

Φ_{inject} and $\eta_{collect}$ are the electron injection efficiency and charge collection efficiency, respectively. $\eta_{collect}$ can be assumed constant as the same semiconductor is being used in the same DSSC with different dye molecules. Φ_{inject} is correlated with the driving force for the electron injection (ΔG_{inject}) and is expressed by

$$\Phi_{inject} \propto f(\Delta G_{inject}) \qquad (11)$$

Therefore, to achieve a higher electron injection efficiency ΔG_{inject} must be more negative. ΔG_{inject} can be evaluated as the difference between the excited state oxidation potential, i.e., the LUMO energy level (E_{OX}^{dye*}) of the dye, and the CB energy level (E_{CB}) of TiO$_2$ ($E_{CB} = -4.0$ eV) and it is stated by

$$\Delta G_{inject} = E_{OX}^{dye*} - E_{CB} \qquad (12)$$

E_{OX}^{dye*} can be estimated using the following equation:

$$E_{OX}^{dye*} = E_{OX}^{dye} - \Delta E \qquad (13)$$

where E_{OX}^{dye} (i.e, $-E_H$) is the ground state oxidation potential of the dye, and ΔE is the vertical electronic transition energy related to λ_c (Table 3). ΔG_{inject} and LHE values are tabulated in Table 6.

All the dyes showed negative ΔG_{inject} values, which facilitates the sufficient driving force for electron injection from the E_{LUMO} of the dye to the CB of TiO$_2$. Also, all the dyes can harness more light and convert into electricity, as the LHE is more than 90% in this study. The V_{OC} of the DSSC can be computed from the empirical eqn (14).

$$V_{OC} = \left| E_H^{Dye} \right| - \left| E_{CB}^{TiO_2} \right| - 0.3 \qquad (14)$$

0.3 is a vital factor appearing from the quasi-Fermi energies of electrons and holes within the HOMO and LUMO energies of the donor and acceptor moieties of the dye.[61] It is to be noted that the kinetics of back-electron transfer was not considered

while computing V_{OC}. These are the indicative values to understand the trend of the V_{OC} of the dyes. The increasing order of calculated V_{OC} is D3 = D1 < D4 < D2. D2 exhibits the highest V_{OC} value, which agrees well with the experimental V_{OC} value and also the trend of the V_{OC}.

Chemical reactivity parameters' study

The molecular energies are obtained for the ionic and neutral species by considering the gas phase geometry using the M06-2X/6-31G(d,p) level of theory. The chemical reactivity parameters,[62] such as ionization potential (IP), electron affinity (A), chemical potential (μ), electronegativity (χ), and electrophilicity index, (ω) were calculated (in eV); the values are presented in Table 7. IP and A were used to calculate the rest of the parameters.

$$\mu = (IP + A)/2 \qquad (15)$$

$$\chi = -(IP + A)/2 \qquad (16)$$

$$\omega = \mu^2/2\xi \qquad (17)$$

ξ is the chemical hardness [(IP − A)/2]. Chemical potential is one of the global quantities, which deals with the escape tendency of an electron cloud, a measure of lowering the energy owing to the highest electron flow between the donor and the acceptor units. Both chemical potential and electronegativity parameters denote the donating ability of the electrons of a molecule.

Therefore, the dye containing higher μ and χ values is expected to perform better in DSSCs. D2 showed higher μ and χ values as compared to the other dyes. Similarly, a higher ω value suggests that the amount of charge transfer from the HOMO to the LUMO is high for D2 and hence the current density for D2 should be high. Therefore, from the chemical reactivity parameter study, it can be inferred that D2 would be the best performing dye for DSSCs.

Adsorption of the dyes onto the TiO$_2$(1 0 1) surface

The adsorption energies of all the dyes are calculated by attaching the dye onto the anatase TiO$_2$(1 0 1) surface using DFT and the optimized geometries of dye anchored TiO$_2$ are given in Fig. 6. There are several modes of adsorption of dyes onto the TiO$_2$ surface, such as monodentate binding, bidentate chelating, and bidentate bridging, which have been proven through an experimental standpoint conventionally accessed by Fourier Transform Infrared (FT-IR) spectroscopy and Surface Enhanced Raman Spectroscopy (SERS).[63]

The different modes (Fig. S5, ESI†) of binding (bidentate bridging, monodentate, and chelating) of the dyes onto the

Table 6 The calculated excited and ground state oxidation potentials (E_{OX}^{dye*} and E_{OX}^{dye}), the electronic vertical transition energies (ΔE) associated with the λ_c, LHE, ΔG_{inject} and open-circuit voltage (V_{OC}) of the dyes

Dye	λ_c/nm	ΔE/eV	E_{OX}^{dye}/eV	E_{OX}^{dye*}/eV	ΔG_{inject}/eV	LHE	V_{OC}/V (theo.)	V_{OC}/V (exp.)
D1	706	1.76	4.99	3.23	−0.77	0.919	0.69	0.50
D2	635	1.95	5.33	3.38	−0.62	0.922	1.03	0.53
D3	696	1.78	4.97	3.19	−0.81	0.909	0.67	0.47
D4	704	1.76	5.12	3.36	−0.64	0.910	0.82	0.47

Table 7 The calculated ionization potential (IP), electron affinity (A), chemical potential (μ), electronegativity (χ), and electrophilicity index (ω) of the dyes

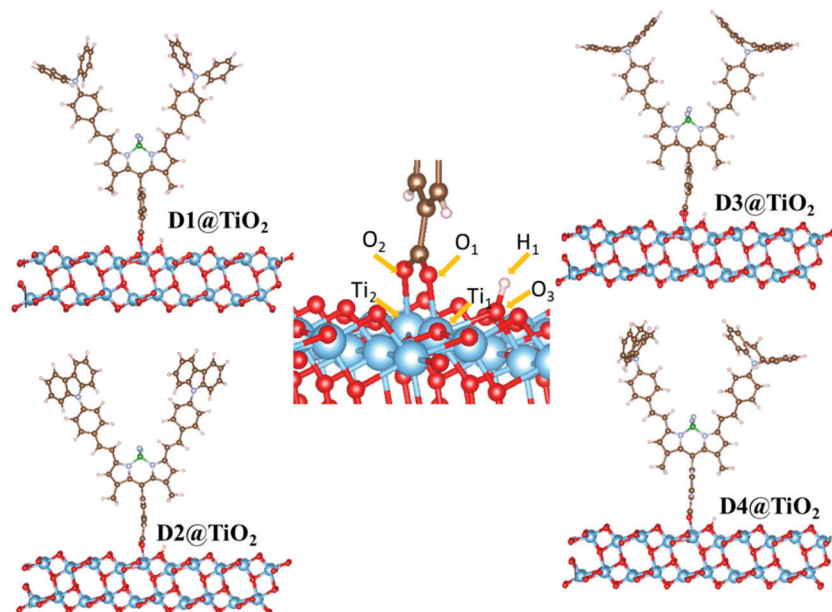| Dyes	IP/eV	A/eV	μ/eV	χ/eV	ω/eV
D1	0.14	−0.19	−3.82	3.82	6.24
D2	0.11	−0.14	−4.07	4.07	6.57
D3	−0.15	−0.15	−3.75	3.75	5.80
D4	−0.12	−0.15	−3.89	3.89	6.19

Fig. 6 Ground state optimized geometries of dyes@TiO$_2$ with an expanded view of the interface between the dyes and the TiO$_2$ surface displaying the bidentate bridging binding of the dye onto the TiO$_2$ surface shown at the center of the figure.

surface of TiO$_2$ were studied to comprehend the adsorption energy. The calculated adsorption energy and distance between Ti and O for the D2 dye have been tabulated in Table S9 (ESI†). The bidentate bridging mode exhibited negative adsorption energy, and the remaining two modes showed positive adsorption energy. Hence the bidentate bridging binding of the dyes onto the surface of TiO$_2$ is more favorable than the other binding modes. Negative adsorption energy indicates the formation of chemical bonds between the dyes and TiO$_2$ and hence the electron injection probability from the LUMO of the dyes to the CB of TiO$_2$ would be better. E_{ads} values are evaluated by using the following equation, and the values are presented in Table 8.

$$E_{ads} = E_{(dye+TiO_2)} - (E_{dye} + E_{TiO_2}) \qquad (18)$$

where E_{dye} and E_{TiO_2} refer to the total energy of the isolated dye and semiconductor, respectively, and $E_{(dye+TiO_2)}$ is the total energy for the dye anchored onto the TiO$_2$ surface. All the dyes showed negative adsorption energies, resulting in chemisorption onto the surface of TiO$_2$ (Table 8).

Density of states (DOS) calculation

To understand the bonding interaction of the dye molecules with the TiO$_2$ surface, the DOS calculations were performed.

The DOS profiles of the TiO$_2$ slab, the partial density of states (PDOS) of the dyes, and TiO$_2$ (in the case of the dyes absorbed onto the surface of TiO$_2$) are plotted in Fig. 7. From DOS of the TiO$_2$(1 0 1) oriented slab, it is clear that the (1 0 1) surface does not lead to any defect states in the bandgap. The bandgap of bulk TiO$_2$ is the same as that of the slab. PDOS of the dye adsorbed surface shows the absence of defect states in the
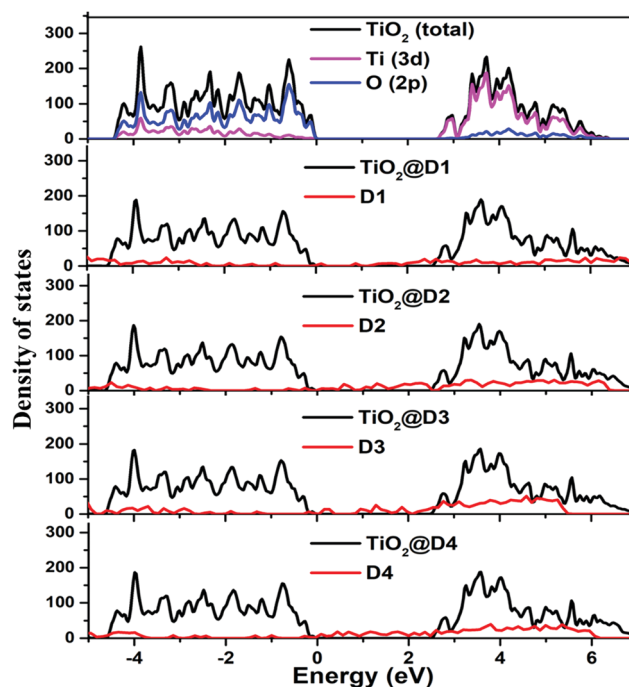

Fig. 7 Partial density of states of TiO$_2$ and dyes + TiO$_2$. For all dyes, when attached to TiO$_2$, a shift in the CBM towards the left is a signature of charge transfer taking place from the dyes to TiO$_2$.

Table 8 Calculated adsorption energies (E_{ads} in eV) and bond lengths (in Å) of the optimized dye structures

Dye	E_{ads}/eV	Ti$_1$–O$_1$/Å	Ti$_2$–O$_2$/Å	d/Å	O$_3$–H/Å
D1	−0.358	2.014	2.095	2.054	0.967
D2	−0.356	2.004	2.097	2.051	0.963
D3	−0.153	2.014	2.087	2.051	0.970
D4	−0.402	1.992	2.064	2.028	0.963

bandgap of TiO_2. The defect states act as trap states, and the absence of such states helps in smooth transfer of electrons from the dyes to TiO_2.

Conclusions

Four BODIPY-based dyes have been investigated using DFT and TD-DFT calculations to understand their photophysical and photoelectrochemical properties. The driving force for dye regeneration was estimated, and D2 possessed the highest values among the other dyes studied in this work. The electron density distribution analysis was performed to understand better the intramolecular charge transfer from the donor to the acceptor moieties, which further correlates with the frontier orbital diagram of the dyes in the ground and virtual states. From the electronic absorption spectra, it can be observed that D2 showed a blue shift as compared with other dyes owing to the poor coplanarity between the carbazole and BODIPY moieties. However, D2 bearing a rigid carbazole unit inhibits intermolecular π–π aggregation, which makes it perform better in DSSCs. The negative adsorption energy of all the dyes indicates that the dyes were chemisorbed onto the (1 0 1) surface of the TiO_2 slab. DOS calculation showed that there is no defect state (trap state) created in the bandgap of TiO_2, which confirms the smooth electron transfer from the dye to the CB of TiO_2. The lowest reorganization energy, highest driving force for dye regeneration, and reasonably higher excited-state lifetime of D2 make it a clear winner among the other dyes, which agrees well with the experimental data reported by Zhang et al.[28] The introduction of a heterocycle to the BODIPY moiety and attachment of donors such as phenothiazine and phenoxazine could make its structure more coplanar and rigid, which would enhance the light-harvesting ability via panchromatic absorption. Our future work is focused on identifying a suitable molecular engineering route to enhance the overall PCE of DSSCs by increasing the driving force for dye regeneration and the photoelectron injection efficiency via tuning the HOMO and LUMO of BODIPY dye molecules.

Conflicts of interest

There are no conflicts to declare.

Acknowledgements

References

1 M. S. Dresselhaus and I. L. Thomas, *Nature*, 2001, **414**, 332–337.

2 M. A. Green, Y. Hishikawa, E. D. Dunlop, D. H. Levi, J. Hohl-Ebinger, M. Yoshita and A. W. Y. Ho-Baillie, *Prog. Photovoltaics Res. Appl.*, 2018, **26**, 3–12.

3 K. Yoshikawa, H. Kawasaki, W. Yoshida, T. Irie, K. Konishi, K. Nakano, T. Uto, D. Adachi, M. Kanematsu, H. Uzu and K. Yamamoto, *Nat. Energy*, 2017, **2**, 1–8.

4 K. Yoshikawa, W. Yoshida, T. Irie, H. Kawasaki, K. Konishi, H. Ishibashi, T. Asatani, D. Adachi, M. Kanematsu, H. Uzu and K. Yamamoto, *Sol. Energy Mater. Sol. Cells*, 2017, **173**, 37–42.

5 Y. K. Eom, S. H. Kang, I. T. Choi, Y. Yoo, J. Kim and H. K. Kim, *J. Mater. Chem. A*, 2017, **5**, 2297–2308.

6 K. Kakiage, Y. Aoyama, T. Yano, K. Oya, J. I. Fujisawa and M. Hanaya, *Chem. Commun.*, 2015, **51**, 15894–15897.

7 T. Kato, A. Handa, T. Yagioka, T. Matsuura, K. Yamamoto, S. Higashi, J. L. Wu, K. F. Tai, H. Hiroi, T. Yoshiyama, T. Sakai and H. Sugimoto, *IEEE J. Photovolt.*, 2017, **7**, 1773–1780.

8 *Nat. Energy*, 2019, **4**, 1.

9 H. Shen, T. Duong, Y. Wu, J. Peng, D. Jacobs, N. Wu, K. Weber, T. White and K. Catchpole, *Sci. Technol. Adv. Mater.*, 2018, **19**, 53–75.

10 M. K. Nazeeruddin, F. De Angelis, S. Fantacci, A. Selloni, G. Viscardi, P. Liska, S. Ito, B. Takeru and M. Grätzel, *J. Am. Chem. Soc.*, 2005, **127**, 16835–16847.

11 H. Hug, M. Bader, P. Mair and T. Glatzel, *Appl. Energy*, 2014, **115**, 216–225.

12 A. Islam, T. H. Chowdhury, C. Qin, L. Han, J. J. Lee, I. M. Bedja, M. Akhtaruzzaman, K. Sopian, A. Mirloup and N. Leclerc, *Sustain. Energy Fuels*, 2018, **2**, 209–214.

13 J. Lim, M. Lee, S. K. Balasingam, J. Kim, D. Kim and Y. Jun, *RSC Adv.*, 2013, **3**, 4801–4805.

14 J. Patwari, S. Sardar, B. Liu, P. Lemmens and S. K. Pal, *Beilstein J. Nanotechnol.*, 2017, **8**, 1705–1713.

15 S. Hattori, K. Ohkubo, Y. Urano, H. Sunahara, T. Nagano, Y. Wada, N. V. Tkachenko, H. Lemmetyinen and S. Fukuzumi, *J. Phys. Chem. B*, 2005, **109**, 15368–15375.

16 H. Klfout, A. Stewart, M. Elkhalifa and H. He, *ACS Appl. Mater. Interfaces*, 2017, **9**, 39873–39889.

17 S. Erten-Ela, M. D. Yilmaz, B. Icli, Y. Dede, S. Icli and E. U. Akkaya, *Org. Lett.*, 2008, **10**, 3299–3302.

18 D. Kumaresan, R. P. Thummel, T. Bura, G. Ulrich and R. Ziessel, *Chem. – Eur. J.*, 2009, **15**, 6335–6339.

19 S. Kolemen, Y. Cakmak, S. Erten-Ela, Y. Altay, J. Brendel, M. Thelakkat and E. U. Akkaya, *Org. Lett.*, 2010, **12**, 3812–3815.

20 S. Kolemen, O. A. Bozdemir, Y. Cakmak, G. Barin, S. Erten-Ela, M. Marszalek, J. H. Yum, S. M. Zakeeruddin, M. K. Nazeeruddin, M. Grätzel and E. U. Akkaya, *Chem. Sci.*, 2011, **2**, 949–954.

21 S. P. Singh and T. Gayathri, *Eur. J. Org. Chem.*, 2014, 4689–4707.

22 Y. Kubo, D. Eguchi, A. Matsumoto, R. Nishiyabu, H. Yakushiji, K. Shigaki and M. Kaneko, *J. Mater. Chem. A*, 2014, **2**, 5204–5211.

23 P. Kele, X. Li, M. Link, K. Nagy, A. Herner, K. Lrincz, S. Béni and O. S. Wolfbeis, *Org. Biomol. Chem.*, 2009, **7**, 3486–3490.

24 H. Choi, J. Ha Lee and J. Hwa Jung, *Analyst*, 2014, **139**, 3866–3870.

25 L. Jean-Gérard, W. Vasseur, F. Scherninski and B. Andrioletti, *Chem. Commun.*, 2018, **54**, 12914–12929.

26 G. D. Sharma, C. G. Athanassios, Z. E. Galateia, N. Agapi and N. Vasilis, *J. Mater. Chem. C*, 2015, **3**, 5652–5664.

27 R. S. Rao, B. Yadagiri, G. D. Sharma and S. P. Singh, *Chem. Commun.*, 2019, **55**, 12535–12538.

28 J. Zhang, F. Lu, S. Qi, Y. Zhao, K. Wang, B. Zhang and Y. Feng, *Dyes Pigm.*, 2016, **128**, 296–303.

29 M. R. Momeni and A. Brown, *J. Chem. Theory Comput.*, 2015, **11**, 2619–2632.

30 S. Chibani, A. D. Laurent, B. Le Guennic and D. Jacquemin, *J. Chem. Theory Comput.*, 2014, **10**, 4574–4582.

31 Q. Huaulmé, C. Aumaitre, O. V. Kontkanen, D. Beljonne, A. Sutter, G. Ulrich, R. Demadrille and N. Leclerc, *Beilstein J. Org. Chem.*, 2019, **15**, 1758–1768.

32 Y. Ooyama, Y. Hagiwara, T. Mizumo, Y. Harima and J. Ohshita, *New J. Chem.*, 2013, **37**, 2479–2485.

33 L. J. He, J. Chen, F. Q. Bai, R. Jia, J. Wang and H. X. Zhang, *Dyes Pigm.*, 2017, **141**, 251–261.

34 S. Mandal, S. Rao and K. Ramanujam, *Ionics*, 2017, **23**, 3545–3554.

35 J. K. Roy, S. Kar and J. Leszczynski, *Sci. Rep.*, 2018, **8**, 1–12.

36 A. Vittadini, A. Selloni, F. P. Rotzinger and M. Grätzel, *J. Phys. Chem. B*, 2000, **104**, 1300–1306.

37 M. K. Nazeeruddin, F. De Angelis, S. Fantacci, A. Selloni, G. Viscardi, P. Liska, S. Ito, B. Takeru and M. Grätzel, *J. Am. Chem. Soc.*, 2005, **127**, 16835–16847.

38 R. Sánchez-De-Armas, J. Oviedo López, M. A. San-Miguel, J. F. Sanz, P. Ordejón and M. Pruneda, *J. Chem. Theory Comput.*, 2010, **6**, 2856–2865.

39 J. P. Sauvage, J. P. Collin, J. C. Chambron, S. Guillerez, C. Coudret, V. Balzani, F. Barigelletti, L. De Cola and L. Flamigni, *Chem. Rev.*, 1994, **94**, 993–1019.

40 K. K. Bando, Y. Mitsuzukz, M. Sungino, K. Sayama and H. Arakawa, *Chem. Lett.*, 1999, 853–854.

41 M. J. Frisch, G. W. Trucks, H. B. Schlegel, G. E. Scuseria, M. A. Robb, J. R. Cheeseman, G. Scalmani, V. Barone, B. Mennucci, G. A. Petersson, H. Nakatsuji, M. Caricato, X. Li, H. P. Hratchian, A. F. Izmaylov, J. Bloino, G. Zheng, J. L. Sonnenberg, M. Hada, M. Ehara, K. Toyota, R. Fukuda, J. Hasegawa, M. Ishida, T. Nakajima, Y. Honda, O. Kitao, H. Nakai, T. Vreven, J. A. Montgomery, J. E. Peralta, F. Ogliaro, M. Bearpark, J. J. Heyd, E. Brothers, K. N. Kudin, V. N. Staroverov, R. Kobayashi, J. Normand, K. Raghavachari, A. Rendell, J. C. Burant, S. S. Iyengar, J. Tomasi, M. Cossi, N. Rega, J. M. Millam, M. Klene, J. E. Knox, J. B. Cross, V. Bakken, C. Adamo, J. Jaramillo, R. Gomperts, R. E. Stratmann, O. Yazyev, A. J. Austin, R. Cammi, C. Pomelli, J. W. Ochterski, R. L. Martin, K. Morokuma, V. G. Zakrzewski, G. A. Voth, P. Salvador, J. J. Dannenberg, S. Dapprich, A. D. Daniels, Ö. Farkas, J. B. Foresman, J. V. Ortiz, J. Cioslowski and D. J. Fox, *Gaussian 09*, 2009.

42 Y. Zhao and D. G. Truhlar, *Theor. Chem. Acc.*, 2008, **120**, 215–241.

43 R. Ditchfield, W. J. Hehre and J. A. Pople, *J. Chem. Phys.*, 1971, **54**, 724–728.

44 W. J. Hehre, K. Ditchfield and J. A. Pople, *J. Chem. Phys.*, 1972, **56**, 2257–2261.

45 N. M. O'Boyle, A. L. Tenderholt and K. M. Langner, *J. Comput. Chem.*, 2007, **29**, 839–845.

46 J. Tomasi, B. Mennucci and R. Cammi, *Chem. Rev.*, 2005, **105**, 2999–3094.

47 L. Thøgersen, J. Olsen, A. Köhn, P. Jørgensen, P. Sałek and T. Helgaker, *J. Chem. Phys.*, 2005, **123**, 1–17.

48 V. Weber, C. J. Tymczak and M. Challacombe, *J. Chem. Phys.*, 2006, **124**, 1–7.

49 G. Kresse and J. Hafner, *Phys. Rev. B: Condens. Matter Mater. Phys.*, 1994, **49**, 14251–14269.

50 G. Kresse and J. Furthmüller, *Phys. Rev. B: Condens. Matter Mater. Phys.*, 1996, **54**, 11169–11186.

51 K. B. John Perdew, *Phys. Rev. Lett.*, 1997, **78**, 1.

52 J. P. Perdew, K. Burke and M. Ernzerhof, *Phys. Rev. Lett.*, 1996, **77**, 3865–3868.

53 F. Han, *Phys. Rev. B: Condens. Matter Mater. Phys.*, 1994, **50**, 17953–17979.

54 G. Kresse and D. Joubert, *Phys. Rev. B: Condens. Matter Mater. Phys.*, 1999, **59**, 1758–1775.

55 S. V. Umale, S. N. Tambat, V. Sudhakar, S. M. Sontakke and K. Krishnamoorthy, *Adv. Powder Technol.*, 2017, **28**, 2859–2864.

56 N. G. Park, J. Van De Lagemaat and A. J. Frank, *J. Phys. Chem. B*, 2000, **104**, 8989–8994.

57 R. A. Marcus, *J. Chem. Phys.*, 1956, **24**, 966–978.

58 A. Einstein, *Phys. Z.*, 1917, **18**, 121–128.

59 K. Chaitanya, X. H. Ju and B. M. Heron, *RSC Adv.*, 2014, **4**, 26621–26634.

60 A. S. Shalabi, A. M. El Mahdy, H. O. Taha and K. A. Soliman, *J. Phys. Chem. Solids*, 2015, **76**, 22–33.

61 R. Maragani, R. Misra, M. S. Roy, M. K. Singh and G. D. Sharma, *Phys. Chem. Chem. Phys.*, 2017, **19**, 8925–8933.

62 V. Abbu, V. Nampally, N. Baindla and P. Tigulla, *J. Solution Chem.*, 2019, **48**, 61–81.

63 C. Anselmi, E. Mosconi, M. Pastore, E. Ronca and F. De Angelis, *Phys. Chem. Chem. Phys.*, 2012, **14**, 15963–15974.